

Fluid-Structure Interactions response of a composite hydrofoil modelled with 1D beam finite elements

A. Faye^{1*}, P. Perali², B. Augier³, M. Sacher², J.-B. Leroux², A. Nême², J.-A. Astolfi¹

¹ Naval Academy Research Institute, IRENav CC600, 29240 Brest Cedex 9, France

² ENSTA Bretagne, IRDL, CNRS UMR 6027, 29200 Brest, France

³ IFREMER, 29200 Brest, France

* Corresponding author: A. Faye, antoine.faye@ecole-navale.fr

ABSTRACT

In this paper, the hydroelastic response of a NACA0015 composite hydrofoil is studied experimentally and numerically. The foil is made of composite materials with fibers not aligned with the span of the foil, which results into the apparition of a bend-twist coupling in the material. Computations are performed using a partitioned approach. The flow problem is solved using a boundary element method (BEM). The structural response of the foil is modelled with two different finite element models. In the first one, the foil is modelled with 2D shell and 3D solid finite elements and in the second model, the foil is modelled with 1D beam finite elements. The experiments are conducted in an open circulation water channel. Hydrodynamic forces and structural displacements are measured for several angles of attack, free stream velocities and submergence depth. This paper shows that the mechanical behaviour of a composite hydrofoil submitted to hydrodynamic loads can be modelled with 1D beam finite elements. This model gives results very similar to a finite element analysis realized with 2D shell and 3D solid finite elements, which are commonly used to model composite structures. The present work also shows that the experimental results can be well predicted by numerical simulations, but it requires a precise modelization of the bend-twist coupling in the materials constituting the foil.

Keywords: Hydrofoil; Equivalent beam; Fluid-Structure Interactions; Composite; Bend-twist coupling.

NOMENCLATURE

c	Chord of the foil [m]
C_l	Lift force coefficient [-]
E_l, E_t	Young modulus along longitudinal and transversal directions [Pa]
\vec{F}	Punctual force to project on a beam element [N]
\vec{F}_1, \vec{F}_2	Nodal forces to apply to the nodes of a beam element [N]
F_{IT}^t	Hydrodynamic forces magnitude acting on the foil at a given iteration [N]
G_{lt}, G_{lf}, G_{tf}	Shear modulus [Pa]
h	Immersion of the foil [m]
IT	Number the current iteration [-]
IT_{min}	Minimal number of iterations for a FSI simulation [-]
\vec{M}_1, \vec{M}_2	Nodal moments to apply to the nodes of a beam element [N]
K	Timoshenko stiffness matrix of a section [N;N.m;N.m ²]
S	Timoshenko compliance matrix of a section [N ⁻¹ ;N ⁻¹ .m ⁻¹ ;N ⁻¹ .m ⁻²]
U	Flow velocity [m/s]
u_{IT}^{tip}	Displacement magnitude of the tip of the foil at a given iteration [m]
x, y	2D coordinates of the shear center of cross-section [m]
ϵ_s	Structural convergence criteria [m]
ϵ_f	Fluid convergence criteria [N]
ν	Poisson coefficient [-]
ρ	Density [kg/m ³]
ξ	Curvilinear abscissa of an arbitrary point of a beam element [-]
AoA	Angle of Attack
BEM	Boundary Element Method
BTC	Bend-Twist Coupling
BTR	Bend-Twist Ratio
FEA	Finite Element Analysis
FEM	Finite Element Method
N_1, N_2	Nodes of a beam element
QS	Quasi-Static
UD	Unidirectional
X	Point of application of a punctual forces
X_p	Point of application of a punctual force projected on a beam element

1. INTRODUCTION

In high performances racing yacht design, hydrofoils are becoming more and more common. To study their performances, Fluid-Structure Interactions (FSI) computations are realized (Liao, Garg, et al. 2019; Mohammed Arab 2020; Temtching Temou 2020). These simulations are mandatory to study high performances hydrofoils because their significant deformations have an impact on the hydrodynamic flow that cannot be neglected.

In the present work a partitioned approach is used. The hydrodynamic loads are obtained using the BEM code *PUFFIn*. The elastic deformation of the foil is computed with the finite element method (FEM), as implemented in *AbaqusTM2022*. Classically, the finite elements used to describe composite hydrofoils are 2D shell elements or 3D solid elements (Liao, Garg, et al. 2019; Liao, Martins, and Y. Young 2021, 2023; Liao, Martins, and Y. L. Young 2019; Mohammed Arab 2020; Temtching Temou

2020). In this work, 1D beam finite elements are considered, which allow a significant computational time reduction. (Faye et al. 2022) shows that a 1D Finite Element Analysis (FEA) is approximately 250 times faster than a 3D FEA. Composite hydrofoils are characterized by anisotropic layup properties. Depending on the fiber orientation in the composite material, couplings between displacements and rotations may be present. For instance, the Bend-Twist Coupling (BTC) has a massive impact on the flow incidence seen by an hydrofoil submitted to an hydrodynamic loading (Lottati 1985; Temtching Temou 2020). For instance, an important BTC can lead to accelerated stall and static divergence ((Y. L. Young et al. 2017)). Modelling foils with 1D beam elements allows to rapidly test several design of foils to avoid such phenomenons. Inversely, numerical models could also be used to design self-regulating foils, where their AoA would be regulated by their deformations and BTC. By doing so, the velocity range where the foils are efficient would be maximized.

To describe the hydroelastic behavior of a foil with a 1D FEA, the three-dimensional geometric non-linear equilibrium analysis of the foil is split into a linear one-dimensional analysis and a set of two dimensional analysis of the cross sections of the foil (Hodges 2006). During the section analysis, 1D structural properties equivalent to the 3D model of the foil are determined. Then, these properties are used to perform the 1D FEA.

The experimental setup and hydrofoil properties are first presented in Section 2. Then, Section 3 details the numerical methods used to model the hydroelastic behaviour of the foil in a flow. Finally, Section 3 discusses the results obtained numerically and experimentally.

2. EXPERIMENTAL SETUP

2.1 Considered foil

The studied foil is straight and prismatic, and its geometry is a NACA0015 section (chord c of 25 cm) extruded over 1.375 m. The dimensions of the foil are detailed in Table 1. The foil is composed of an Airex web foam, a ply of glass-epoxy taffeta and an unidirectional (UD) glass-epoxy ply. The taffeta ply behavior is assumed to be orthotropic with 1 and 2 directions respectively parallel to the warp and weft directions. For the UD ply, a transverse isotropic behavior is assumed, with the 1 direction parallel to the fiber. The cross section of the foil is illustrated in Figure 2 and the engineering elastic constants of the materials constituting the foils are presented in Tables 2 and 3.

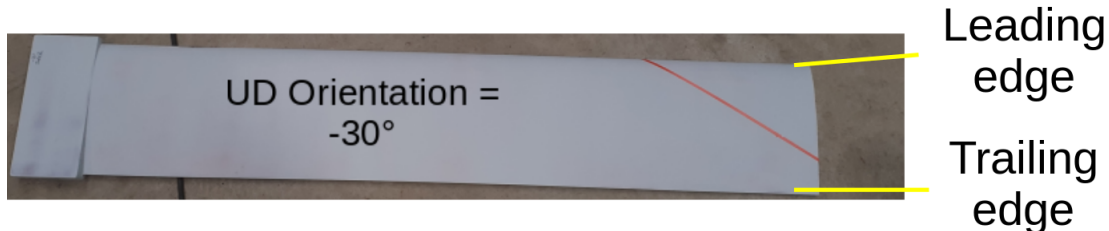


Figure 1: Example of a figure.

Figure 1 shows the studied foil, with a orange color mark to symbolize the orientation of the fibers in the UD ply. The angle between the leading edge of the foil and the fibers is -30° . Because the fiber are not aligned with the span of the foil, there is a bend-twist coupling in the foil. The BTC leads to a nose-up twist angle. When the foil is bent by the hydrodynamic loading, the nose-up twist angle

increases its angle of attack (AoA) with respect to the flow. Therefore, the hydrodynamic loads of the foil increases when it is deformed.

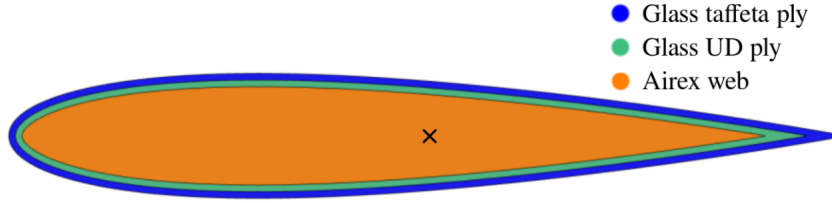


Figure 2: Cross section of the foil.

Table 1: Geometric properties of the foils.

Chord (m)	Span (m)	Taffeta ply thickness (mm)	UD ply thickness	UD Orientation (deg)
0.250	1.375	9.45E-02	3.27E-01	-30

Table 2: Engineering constants of the materials constituting the skin of the foils.

Material	E_1 (GPa)	E_2 (GPa)	ν_{12}	G_{12} (GPa)	G_{13} (GPa)	G_{23} (GPa)	ρ (kg/m ³)
Taffeta	16.0	16.5	0.108	1.81	0.9	0.9	1625
UD	27.4	5.1	0.348	1.81	1.81	0.9	1625

Table 3: Mechanical properties of the Airex web.

Material	E (MPa)	ν	ρ (kg/m ³)
Airex Foam	25.0	0.400	60

2.2 Ifremer Flume Tank

The experimental campaign is realised at the current circulating tank of Ifremer, located in Boulogne-sur-Mer (France). The flume tank, illustrated in Figure 3, is 18 m long, 4m wide and 2 m high. It generates a current, considered uniform, with velocities ranging from 0.1 to 2.2 m/s. In the present study, the considered velocities U are 0.8 m/s and 1.2 m/s, respectively associated to Froude numbers of 0.51 and 0.77, considering the chord of the profile as the reference length. The turbulence intensity of the flow is considered constant with a value of 1.5 %.

The foil is inserted in a clamping system and a 6-DOF hexapod allows to change the angle of attack α and the immersion of the foil h . The rotation axis and reference point for the immersion are located at midchord of the non-deformed hydrofoil.

The hydrodynamic loads acting on the foil are measured with a balance fixed at the hexapod. The balance. The sensor measures the three orthogonal force and moment components, respectively with a range of 150 DaN and 100 DaN.m. The precision of the balance is about 1.5 N for the forces and 1 N.m for the moments. To measure only the forces acting on the hydrofoil, the forces measured with the clamping system alone are subtracted to the measurements.

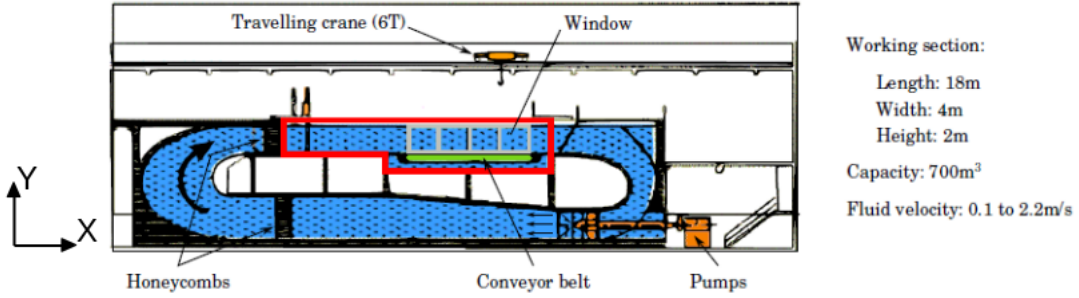


Figure 3: Scheme of the Ifremer Flume Tank (adapted from (Marty et al. 2021))

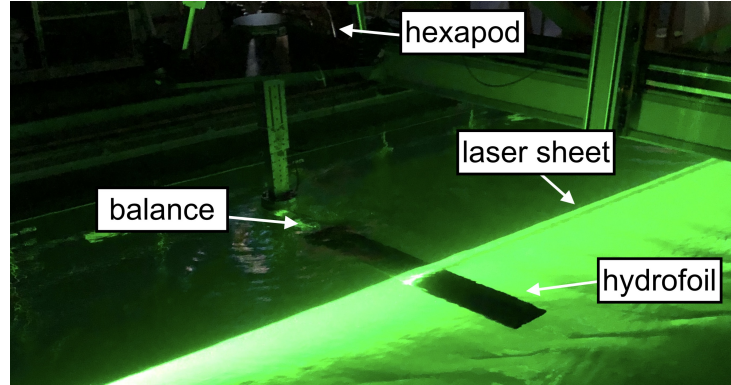


Figure 4: Laser sheet projected on the foil viewed at the top of the flume tank.

As shown on Figure 4, a laser sheet is used to illuminate a section of the foil located at 1.19 m from the clamping. Images of the illuminated section are recorded using a high speed camera for the different angles of attack, immersion depths and flow velocity. Assuming that the foil section undergoes rigid displacements and rotations, an edge detection algorithm and a least square interpolation allow to get the positions of the section in the vertical plane. Subtracting the position of the section at rest, it is finally possible to estimate the bending displacements and twist angles due to the hydrodynamic loads.

3. NUMERICAL MODELS

3.1 Flow Model

In this section, a brief description of the fluid solver *PUFFIn* is proposed. The fluid problem is solved with a Boundary Element Method (BEM) for potential flow. The viscous effects are neglected and the flow is supposed to be irrotational and incompressible. The velocity field $\mathbf{u}(\mathbf{x}, t)$ is the superposition of the undisturbed flow \mathbf{U}_0 and the gradient of a disturbance potential $\phi(\mathbf{x}, t)$ satisfying a Laplace equation:

$$\Delta\phi(\mathbf{x}, t) = 0 \quad (1)$$

Using the second Green identity, this equation is equivalent to a boundary integral equation on the domain boundaries ((Katz et al. 2001)), i.e. of the hydrofoil surface S_H , the free surface boundary

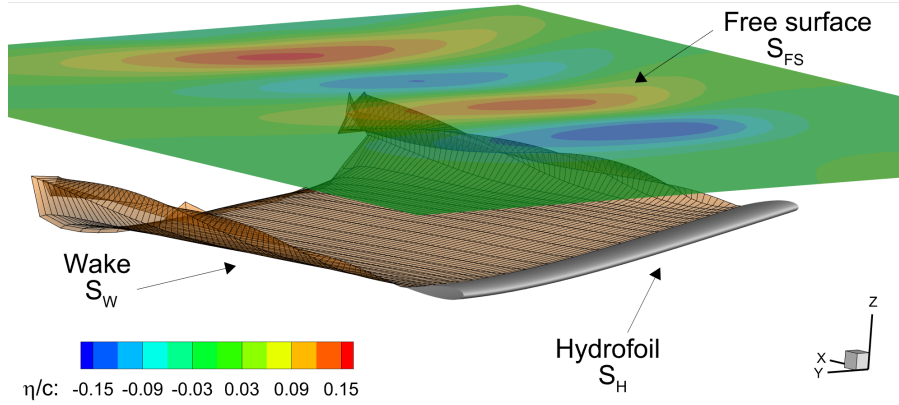


Figure 5: Boundary surfaces of the potential flow problem.

S_{FS} and the wake surface S_W (Figure 5):

$$\phi = \frac{1}{4\pi} \int_{S_H + S_{FS}} \left[\frac{\partial \phi}{\partial n} \frac{1}{r} - \phi \frac{\partial}{\partial n} \left(\frac{1}{r} \right) \right] dS - \frac{1}{4\pi} \int_{S_W} \left[\phi \frac{\partial}{\partial n} \left(\frac{1}{r} \right) \right] dS \quad (2)$$

with \mathbf{n} the outward pointing normal vector. Additional boundary conditions are needed to solve the boundary integral equation. On the hydrofoil, the non-penetration condition imposes:

$$\frac{\partial \phi}{\partial n} = \mathbf{U}_0 \cdot \mathbf{n} \quad (3)$$

In addition, the linearized condition of Neumann-Kelvin ((Newman 2018)) is imposed on the undisturbed free surface location ($z = 0$):

$$(\mathbf{U}_0 \cdot \nabla)^2 \phi + g \frac{\partial \phi}{\partial z} = 0 \quad (4)$$

The free surface elevation is obtained from the Bernoulli relation on the initial free surface:

$$\eta = - \frac{\mathbf{U}_0 \cdot \nabla \phi}{g} \quad (5)$$

A Lagrangian approach is used to iteratively construct the wake surface during the computation. For inviscid flow, the potential on a wake panel convected by the flow should remain constant. Thus, the distribution of the potential ϕ on the wake can be obtained using a Kutta condition, imposing the equality of the extrados and intrados pressure at the trailing edge.

To construct a numerical solution, the boundaries are discretized using quadrilateral elements and the potential is supposed to be constant on each element. More details on the theory and implementation can be found in the (*PUFFIn documentation 2023*). The pressure distribution on the hydrofoil is obtained with the Bernoulli relation. Integration of the pressure over the surface S_H gives the hydrodynamic forces and moments acting on the hydrofoil.

In this work, the free surface extends 2.5 chords upstream the hydrofoil and 7.5 chords downstream. The free surface length in the spanwise direction is more than two times the hydrofoil span. A grid convergence study (not shown for the sake of concision) was performed to select an appropriate number of panels for the hydrofoil and free surface discretization. The free surface is discretized using 140 panels in the streamwise direction and 28 panels in the spanwise direction. This ensures that a wave length corresponds to at least 20 panels. For the hydrofoil, 100 panels are used in the chord direction and 24 panels are used along the span.

3.2 3D Finite Element Model of the foils

To compute the structural response of the foil, two finite element models are considered. In this Section, the 3D finite element model of the foil, referred as *Abaqus 3D* in the paper, is presented.

In the 3D Abaqus FEA, the foil is decomposed in two parts, a first one containing the Airex foam, meshed with 3D solid elements. The second part is meshed with 2D shell elements and represents the composite skin of the foil. The 2D shell elements used to model the UD and taffeta plies drastically reduce the size of the mesh, because the skin is not discretized along its thickness. The 3D solid elements used to model the Airex web are 8 node brick elements C3D8R. A mesh sensitivity analysis has been performed to provide the optimal number of elements to correctly capture the behavior of the foils. The optimal number of solid elements to mesh the web is approximately 700 000 element, such a mesh is illustrated in Figure 6. For the skin of the foil, the optimal number of elements is 60 000 (see Figure 6).

The elements used to mesh the skin are triangular Kirchhoff shell elements, denoted STRI3 in Abaqus™. On these elements, a composite layup is defined to specify the thickness of the layers and the fiber orientations. A Tie constraint is also defined to link the skin to the web. This constraint imposes the surface of the web to have the same motion as the 2D skin of the foil. Finally, to model the clamping of the heel of the foil, the displacements of the skin and the web are constrained to be null in $Z = 0$ m.

The forces acting on the foil are the gravity and the hydrodynamic loading induced by the flow. The gravity loads to apply on each elements are computed in Abaqus™ from the volume of the elements and the density of the materials (see Table 2 and 3).

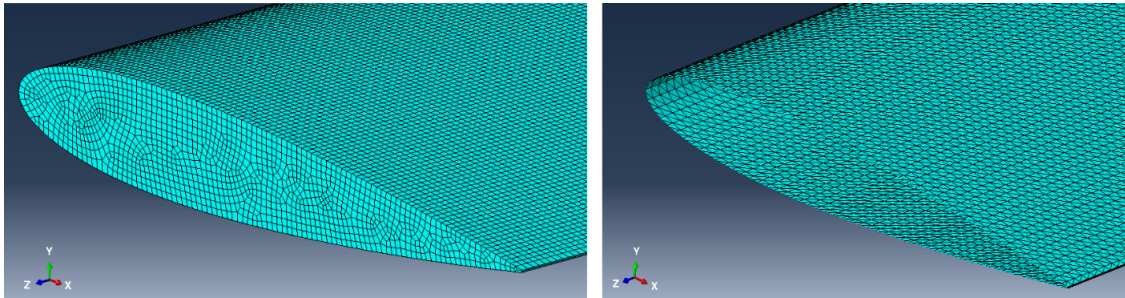


Figure 6: Structural meshes of the web of the foil (left) and of the skin of the foil (right).

3.3 1D Finite Element Model of the foils

In this section, the 1D finite element model of the foil is presented, it is referred as *Abaqus 1D* in the rest of the paper. To characterize the mechanical behavior of a foil with equivalent beam elements, the 3D structural problem is decomposed into a set of 2D section analysis and a 1D nonlinear FEA. To do so, the main steps are :

1. Evaluation of the structural properties of sections composing the foils (2D problems);
2. Reconstruction of equivalent beam elements;
3. 1D Finite Element Analysis (1D problem);

4. Reconstruction of 3D displacements from the results obtained with the equivalent beam model.

The first step is to characterize the structural properties of the sections along the foil span. The difficulty of this step is to find equivalent properties of an anisotropic and heterogeneous composite section. As a starting point, a 3D geometry is defined with different regions for each materials (UD, taffeta and Airex in the present work). This geometry is then cut in several sections along its span, as illustrated in Figure 7. Obviously, for a prismatic foil, a single cut is required because the section is constant along its span. The number of cuts should be adapted according to the variations of the geometric and elastic properties of the foil along its span.

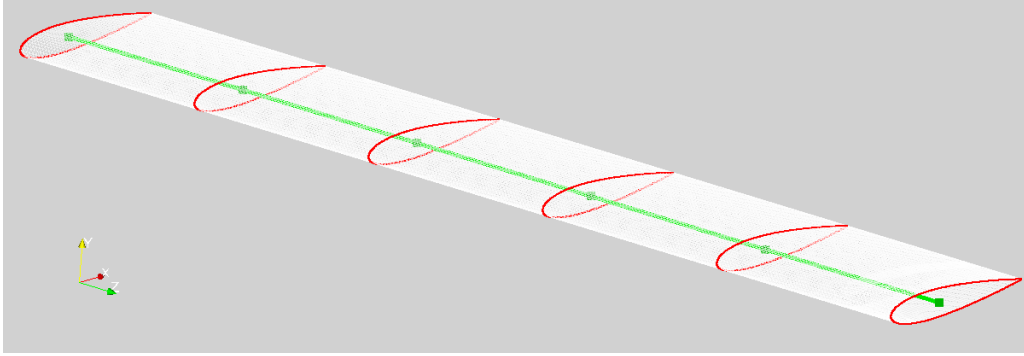


Figure 7: Illustration of the studied foil with six cuts.

A centerline has to be defined for the equivalent beam, this line goes through the shear centers of each section. The computation of the shear center is done during the next step, which is the section analysis. The shear center of the section can be computed from the terms of the compliance matrix S , defined as the inverse of the stiffness matrix K as shown in (Hodges 2006). For this step, the section is meshed and its elastic properties are integrated over its surface. The method proposed in (Han et al. 2015) is presently used.

Actually, two section analysis are required, a first one to compute the shear center of the section and a second one to evaluate the equivalent properties of the section at the shear center. For the first analysis, the section properties are computed according to an arbitrary origin (the leading edge of the foil in the present work). From this analysis, a first Timoshenko stiffness matrix is obtained from which the shear center is finally computed. This stiffness matrix relates the forces applied on the section to its strains, such as:

$$\begin{pmatrix} F_1 \\ F_2 \\ F_3 \\ M_1 \\ M_2 \\ M_3 \end{pmatrix} = \begin{pmatrix} K_{11} & K_{12} & K_{13} & K_{14} & K_{15} & K_{16} \\ K_{12} & K_{22} & K_{23} & K_{24} & K_{25} & K_{26} \\ K_{13} & K_{23} & K_{33} & K_{34} & K_{35} & K_{36} \\ K_{14} & K_{24} & K_{34} & K_{44} & K_{45} & K_{46} \\ K_{15} & K_{25} & K_{35} & K_{45} & K_{55} & K_{56} \\ K_{16} & K_{26} & K_{36} & K_{46} & K_{56} & K_{66} \end{pmatrix} \begin{pmatrix} \gamma_{11} \\ \gamma_{12} \\ \gamma_{13} \\ \kappa_1 \\ \kappa_2 \\ \kappa_3 \end{pmatrix} \quad (6)$$

The subscripts 1, 2 and 3 used in the present coordinate system (see Figure 7), are respectively related to the z, x and y directions. The matrix in Eq. 6 is representative of the equivalent mechanical properties of the analyzed cross section. K_{45} and K_{46} terms quantify the intensity and the sign of the BTC. In AbaqusTM, the cross sections are meshed with triangular elements WARP2D3, that capture

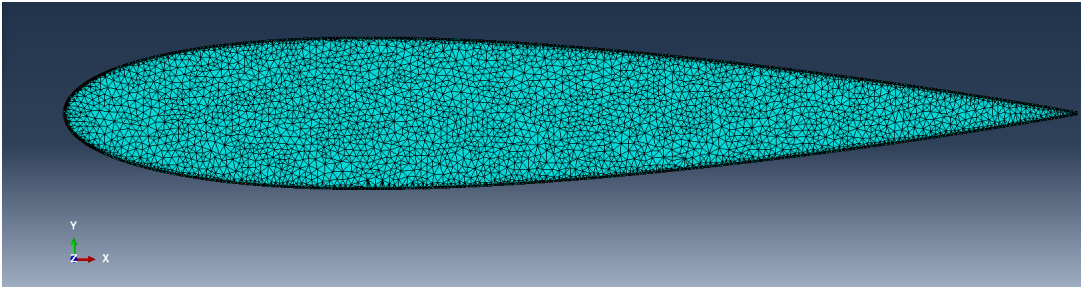


Figure 8: Triangular mesh of the cross section of a foil.

the anisotropic properties of the materials composing the sections of the foils. The optimal mesh is determined with a mesh sensitivity analysis where the cell sizes are decreased until convergence of the terms of K . A converged mesh of the section is shown in Figure 8.

After the section analysis, beam elements are reconstructed and assembled to describe the foil as an assembly of 1D beam elements. The foil is modelled with B31 beam elements in Abaqus™, which are linear Timoshenko beam elements. The structural properties of the beam elements are determined from the section Timoshenko matrix K and the geometry (length, orientation) of the beam elements.

As in *Abaqus 3D*, the displacement of the node located in $Z = 0$ m are fixed to 0 and the loads are decomposed into a gravity component and a fluid component. To apply the gravity in *Abaqus 1D*, nodes going through the centers of mass of the sections are defined, their number and position along the span are the same as the nodes of the equivalent beam elements.

The nodes going through the centers of mass are rigidly linked to their closest beam nodes and are submitted to punctual loads corresponding to the weight of the foil. For a given node, the gravity load is computed from the lineic mass of the foil and the half-lengths of the elements linked to this nodes (only one element for the extremity nodes).

3.4 Coupling strategies

In this Section, the coupling strategies considered to realize FSI simulations with *PUFFIn* and *Abaqus 1D* or *Abaqus 3D* are presented. The coupling strategies are similar, the differences occurs when the fluid forces are transmitted to the structural solver and when the fluid mesh is deformed.

The iterative FSI coupling is explicit and Quasi-Static (QS), which means that, at each iteration, the system is considered at static equilibrium. With this kind of coupling, the acceleration of the foil and the added mass effect are not considered to compute the deformation of the foil. Figure 9 shows the organizational charts of the two couplings. The communication between the fluid and structural solver is realized with *Python* scripts.

The main steps of the two couplings are similar, the computation begin with an initial fluid computation on the undeformed geometry of the foil to determine a pressure field at the surface of the foil. Then, the iterative process begins, the deformation of the foil due to the pressure field is computed.

The static structural problem is solved using an iterative Newton-Raphson method, to take into account the non-linear geometrical effects. After the FEA, the fluid mesh is deformed according to the deformation of the foil and a new *PUFFIn* computation is performed. The two last steps are then repeated until convergence.

Two convergence criteria are defined, ϵ_s and ϵ_f , respectively for the structure and the fluid forces. ϵ_s is defined as the difference between the displacement of the tip of the foil at the current and previous iteration, u_{IT}^{tip} is the norm of the displacement vector of the tip of the foil.

At the end of an iteration, ϵ_f is computed as the difference between the hydrodynamic force magnitude acting on the foil at the current and previous iteration. F_{IT} is the magnitude of the fluid forces at the current iteration. A minimum number of iteration IT_{min} is defined to check the convergence of the simulation. At the end of a fluid computation on a deformed foil geometry, if the number of structural iterations IT is higher than IT_{min} and the hydrodynamic loading and displacements of the foil are converged, the computation stops, otherwise, a new iteration is performed.

For the considered foil, a typical number of iterations to reach convergence of fluid forces and displacements is about 5. At the end of the computation, the outputs are the shape of the deformed foil, the associated pressure field and the total hydrodynamic forces and moments acting on the foil.

3.4.1 Abaqus 3D

In the coupling *PUFFIn/Abaqus 3D*, the pressure field given by PUFFIn is applied on the surface of the foil. Because the fluid mesh is coarser than the structural mesh, the pressure field given by *PUFFIn* is interpolated on the Abaqus mesh with a distance weighting algorithm.

After the FEA, *Abaqus 3D* returns the displacement field of the surface of the foil expressed at the nodes of the structural mesh. Because this mesh does not match with the fluid one, a second interpolation is realized. Radial Basis Function (RBF) are used to compute the displacements of the fluid mesh nodes from the displacements of the structural mesh nodes.

Each structural computation in Abaqus™ begins with the undeformed foil. Therefore, the pressure field given by *PUFFIn* on a deformed fluid mesh is expressed on the undeformed fluid mesh before the interpolation.

3.4.2 Abaqus 1D

In the coupling *PUFFIn/Abaqus 1D*, a 3D pressure field is projected on the equivalent beam elements. To do so, the pressure field is expressed as a punctual force field from the centers, the area vectors and the pressure at the fluid faces. Then, for each application point of the punctual forces, the closest beam element is determined. The punctual forces is distributed on the two nodes of the corresponding beam element.

Figure 10 illustrates the projection method, in this Figure, the beam element is defined between the nodes N_1 and N_2 and a punctual force \vec{F} is applied at point X . The point X_p is defined as the projection of X on the beam element, X_p is used to define the adimensionnal parameter ξ used to distribute the load on the nodes N_1 and N_2 (see Eq. 7).

$$\xi = \frac{\|\overrightarrow{N_1 X_p}\|}{\|\overrightarrow{N_1 N_2}\|} \quad (7)$$

The punctual force F is distributed between the nodes of the beam element accordingly to the value

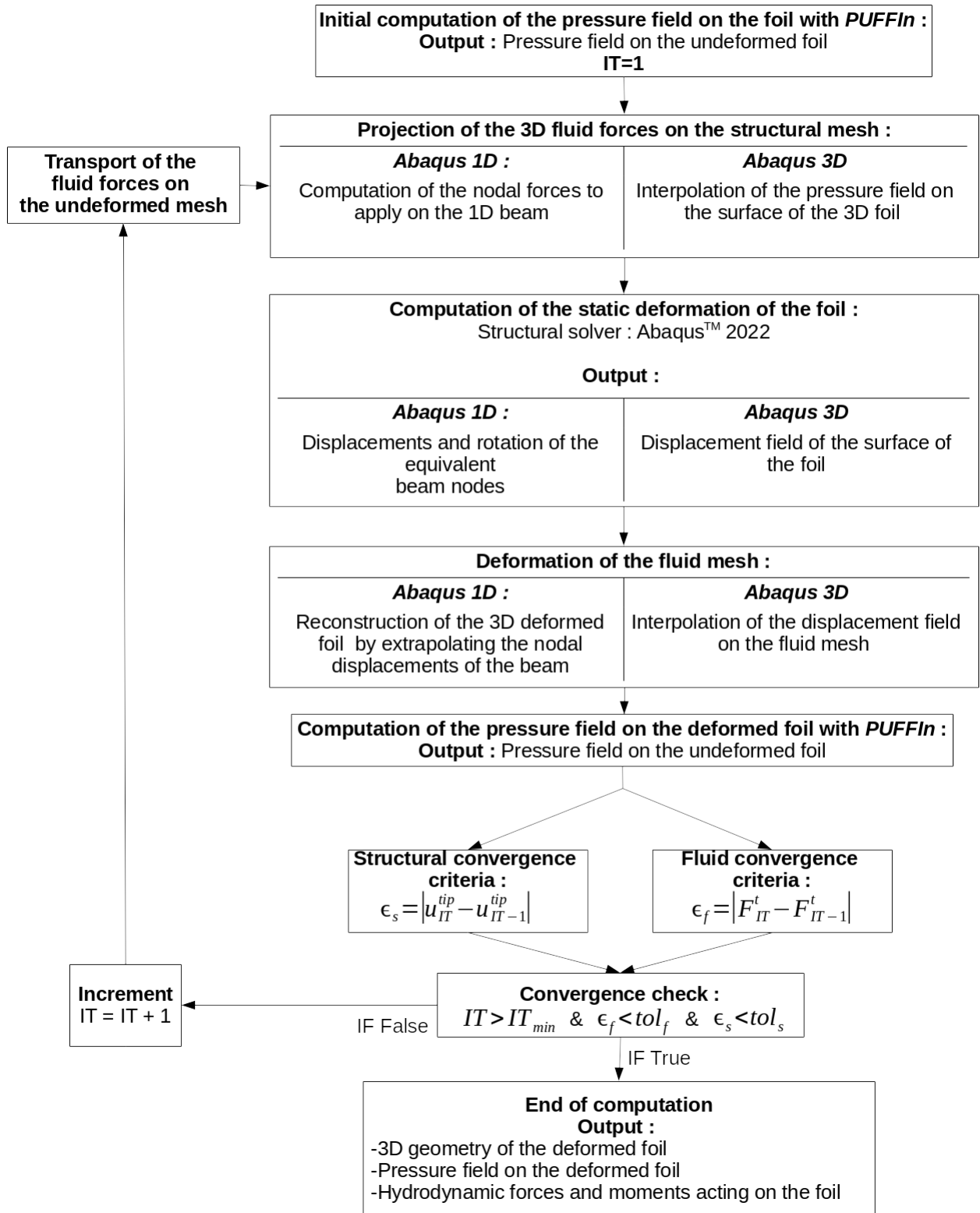


Figure 9: Organizational chart of the couplings *PUFFIn/Abaqus 3D* and *PUFFIn/Abaqus 1D*.

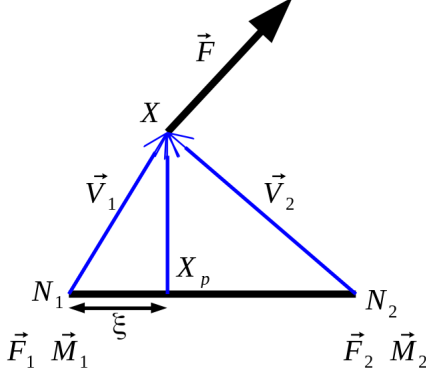


Figure 10: Illustration of the force projection method.

of ξ . In Figure 10, \vec{F}_1 and \vec{F}_2 are the nodal loads respectively applied on N_1 and N_2 during the FEA. The nodal forces are defined as:

$$\vec{F}_1 = (1 - \xi) \vec{F} \quad (8)$$

$$\vec{F}_2 = \xi \vec{F} \quad (9)$$

To compute the nodal moments, defined as \vec{M}_1 and \vec{M}_2 in Figure 10, the vector \vec{V}_1 and \vec{V}_2 are respectively defined as $\vec{N}_1\vec{X}$ and $\vec{N}_2\vec{X}$. The nodal moments are computed such as :

$$\vec{M}_1 = \vec{V}_1 \wedge \vec{F}_1 \quad (10)$$

$$\vec{M}_2 = \vec{V}_2 \wedge \vec{F}_2 \quad (11)$$

To avoid any problem of fluid faces overlapping several beam elements, the fluid mesh is refined according to the 1D structural mesh before the beginning of the iterative FSI loop. To do so, 2D planes perpendicular to the centerline of the beam elements are defined at the beam nodes. The faces of the fluid mesh intersected by these plane are cut in sub-faces in order to have a correct projection of the fluid forces on the beam elements.

After the computation of the static deformation of the foil, the fluid mesh is deformed accordingly. To do so, the shape of the deformed 3D foil is extrapolated from the nodal displacements of the beam computed during the FEA. To reconstruct a 3D deformed geometry, each of its points is projected on the closest beam element. During the projection of a point of the 3D geometry on a beam elements, two cases can be encountered:

1. The point is projected on a node of a beam element \rightarrow its displacement is computed from the associated nodal displacement;
2. The point is projected on a arbitrary point of a beam element \rightarrow its displacement is computed from the displacements of the nodes of the associated beam element with the linear shape functions of a Timoshenko beam element (see (Oñate 2013)).

With this approach, the sections of the foil have a rigid body motion and their deformations are not considered to reconstruct the deformed shape of a foil.

As in the coupling *PUFFIn/Abaqus 3D*, the structural computations always begin with the foil in its undeformed configuration. Therefore, the pressure forces projected on the foil have to be expressed on the undeformed mesh of the foil. To do so, the points of application of the forces (X in Figure 10) are considered constant during the FSI loop and they are equal to the centers of the faces of the undeformed beam mesh. However, the forces \vec{F} are computed from the current fluid mesh, which means that the orientations of the forces changes when the foil is deformed.

4. RESULTS AND DISCUSSION

4.1 Fixed depth

In this Section, the behavior of the foil is studied experimentally for two flow velocities, $U = 0.8$ m and $U = 1.2$ m. The depth of the foil is chosen to minimize the free surface effects. In the flume tank, the maximal immersion possible is $h/c = 2.76$, which corresponds to a depth of 0.69 m for the considered foil.

The objective is to study the behavior of the foil for several AoA for the two considered flow velocities. The hydrodynamic forces are computed thanks to the scale fixed to the hexapod (see Section 2.2). The force computed on the foil are relative to the configuration where the foil is immersed in the flume tank without any current. This means that the forces values presented in this Section does not take into account the buoyancy of the foil. In addition to the hydrodynamic forces, the vertical displacement and torsion angle induced by the flow are also measured. The displacement and torsion of the foil are also computed relatively to the reference configuration without any flow, meaning that the displacements measured are only induced by the dynamic pressure of the fluid and not the buoyancy of the foil. Their values are plotted for different AoA in Figure 11.

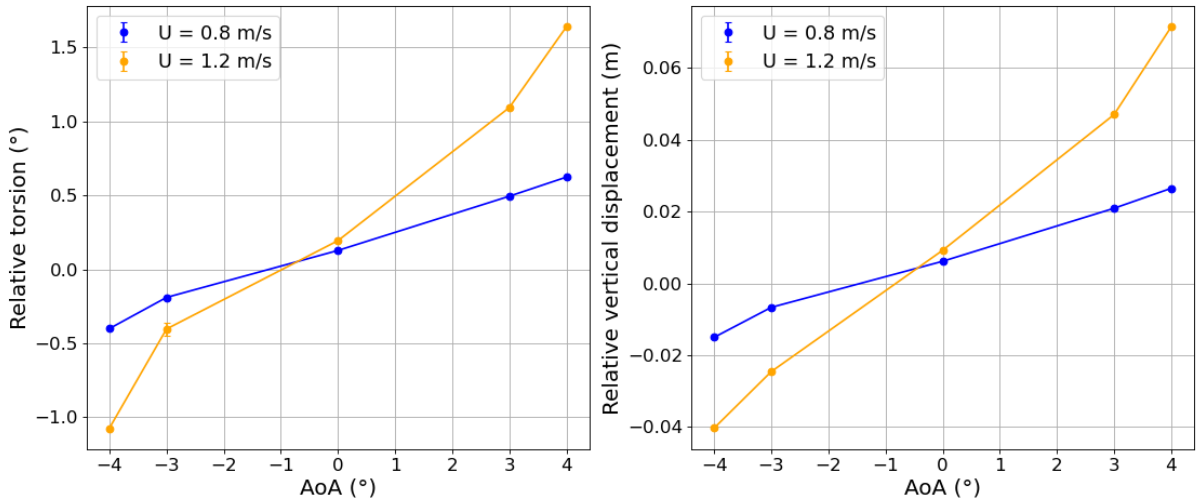


Figure 11: Experimental values of the torsion (left) and vertical displacement (right) of the foil at $h/c = 2.76$.

Figure 11 shows that for an AoA of 0° , the displacement and torsion of the foil are not null. This is because the foil is initially bent because of its buoyancy. Because of the BTC, the flexion of the foil due to buoyancy induces a torsion angle which increases the AoA of the foil. Therefore, for an AoA of 0° , the buoyancy of the foil induces a positive AoA. This is why the angle for which the displacements are null is negative. To have no deformations of the foil, its initial AoA must be negative in order to compensate the positive AoA due to buoyancy.

Figure 11 shows the impact of a nose-up twist angle on the behavior of the foil. The nose-up twist angle tends to increase the lift coefficient of the foil as it is deformed. To highlight this, the ratio between the lift coefficient at the AoA of 4° and 3° can be compared to the theoretical ratio considering no nose-up twist angle. If there is no nose-up twist angle, the lift coefficient remains constant when the foil is deformed. For small AoA, the lift coefficient is assumed to be a linear function of the AoA. The vertical displacement of the foil is also considered to be a linear function of the lift. Therefore, an increase of 33% is expected when the AoA goes from 3° to 4° . However, for $U = 1.2$ m/s, the increase is about 52%, this is due to the nose-up twist angle, which increases the lift coefficient of the foil when it is deformed. This phenomenon is less clearly visible for the velocity of 0.8 m/s because the hydrodynamic loads induced by the flow are lower and therefore the deformation of the foil is lower.

Figure 12 shows the values of the hydrodynamic forces acting on the foil for the two velocities considered. The zero lift AoA is negative despite the symmetry of the profile. As explained earlier, a positive AoA is induced by the bending due to the buoyancy of the foil.

In Figure 12, the lift coefficient magnitude is higher for the speed of 1.2 m/s. Because the lift is higher for the velocity of 1.2 m/s than for the velocity of 0.8 m/s, the flexion of the foil is more bent, resulting into a higher AoA because of the BTC. This phenomenon is more visible for high AoA, because they leads to important deformations and thus the BTC induces a more significant nose-up twist angle.

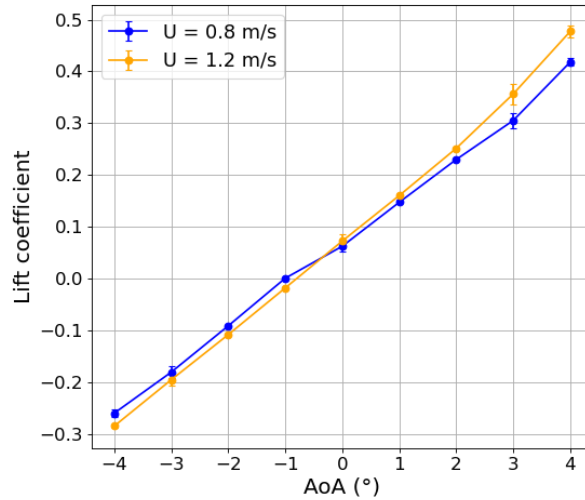


Figure 12: Experimental values of the lift coefficient of the foil at $h/c = 2.76$.

The results show the impact of the nose-up twist angle, which leads to higher lift coefficients for the velocity of 1.2 m/s, if the lift induces a sufficient deformation. The nose-up twist angle also increases the deformation of the foil, whereas there would be decreased if the sign of the BTC was opposite.

4.2 Influence of the immersion

In this Section, the influence of the immersion of the foil on its lift and deformation is investigated for a fixed AoA. To maximize the deformation of the foil, an AoA of 4° is considered. With the hexapod of the Ifremer flume tank, the immersion of the foil are fixed at $h/c = [0.5; 0.75; 1; 2.76]$.

Figure 13 shows the influence of the immersion of the foil on the lift coefficients. The effect of the free surface on the foil is different for the two considered velocities. For the lower Froude configuration

($U = 0.8$ m/s), the lift coefficient increases when the immersion is decreasing, until $h/c = 1$, which corresponds to the point where the wave created by the foil surges. Then, there is a massive loss of lift. For the higher Froude configuration ($U = 1.2$ m/s), the lift is reduced when the foil is getting near the free surface. As for the velocity of 0.8 m/s, a massive loss of lift occurs when h/c is lower than 1, which reflects the surge of the free surface above the foil. The reduction of the lift is higher for $U = 1.2$ m/s because the associated surge is more important.

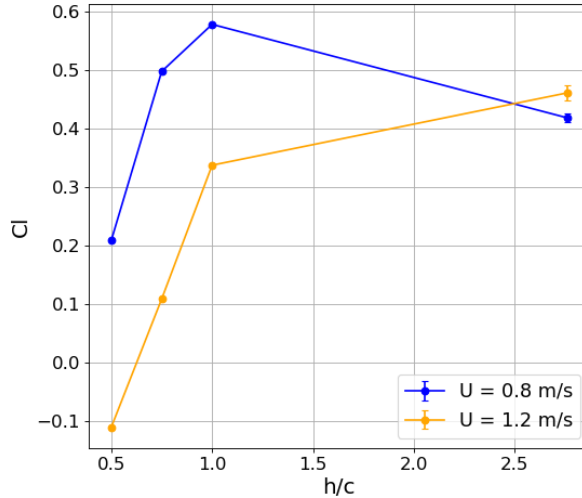


Figure 13: Experimental values of the lift coefficient at $\text{AoA} = 4^\circ$.

Figures 14 shows the experimental measures of torsion and vertical displacement of the foil as a function of the immersion of the foil. As in Section 4.1, the torsion and vertical displacement follows similar tendencies, which can be related to the lift of the foil. The results show that the deformation of the foil far from the free surface are higher for the velocity of 1.2 m/s, which is expected because the lift is higher in this case. For the lower Froude configuration, Figure 14 shows that the vertical displacement is maximum for $h/c = 1$, which is coherent with the evolution of the lift coefficient presented in Figure 13. A similar observation can be done for the higher Froude configuration, where the deformation of the foil are maximum for $h/c = 2.76$ and decreasing when it is closer to the free surface. Figures 14 also shows the loss of lift for low immersion, resulting into an important reduction of the deformation of the foil.

The experimental measures shows that the behavior of the foil near the free surface is Froude-dependent. For the lowest Froude configuration, an increase of the lift of the foil occurs when it is getting closer to the free surface, this phenomenon is due to an augmentation of the depression at the extrados of the foil, which disappears when the free surface above the foil surges. For the higher Froude configuration, the lift decreases with the immersion and, as for the lower Froude configuration, there is a massive loss of lift for low immersion, which corresponds to the surging of the wave induced by the foil.

4.3 Validation of numerical models

In this section, results obtained with the numerical models are confronted to the experimental results. The foil is tested for the maximum immersion ($h/c = 2.76$) and a velocity of $U = 0.8$ m/s. Various AoA have been tested, from -4° to 4° . Figure 15 shows the torsion and vertical displacements computed

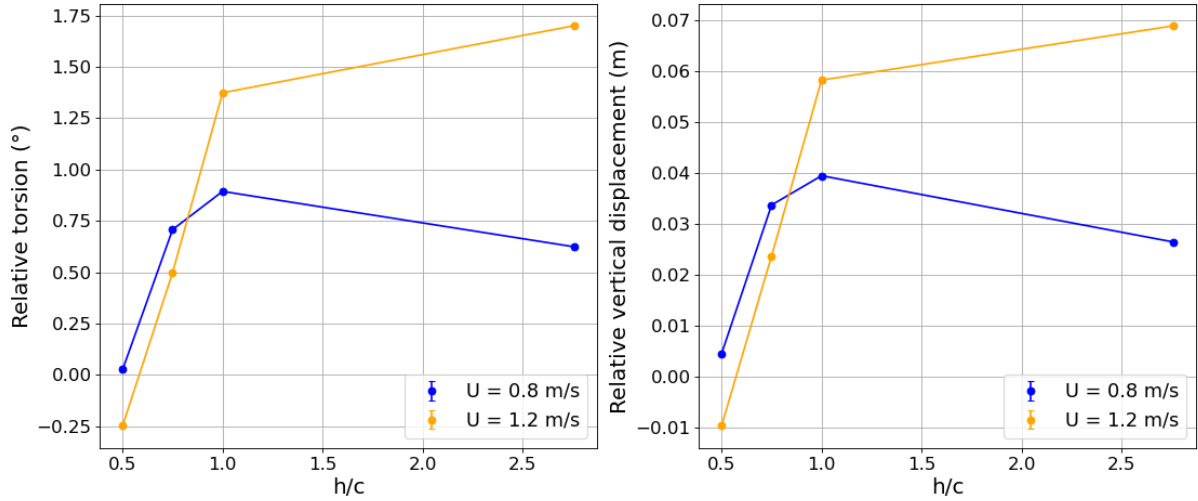


Figure 14: Experimental values of the torsion and vertical displacement of the foil at $\text{AoA} = 4^\circ$.

numerically and experimentally.

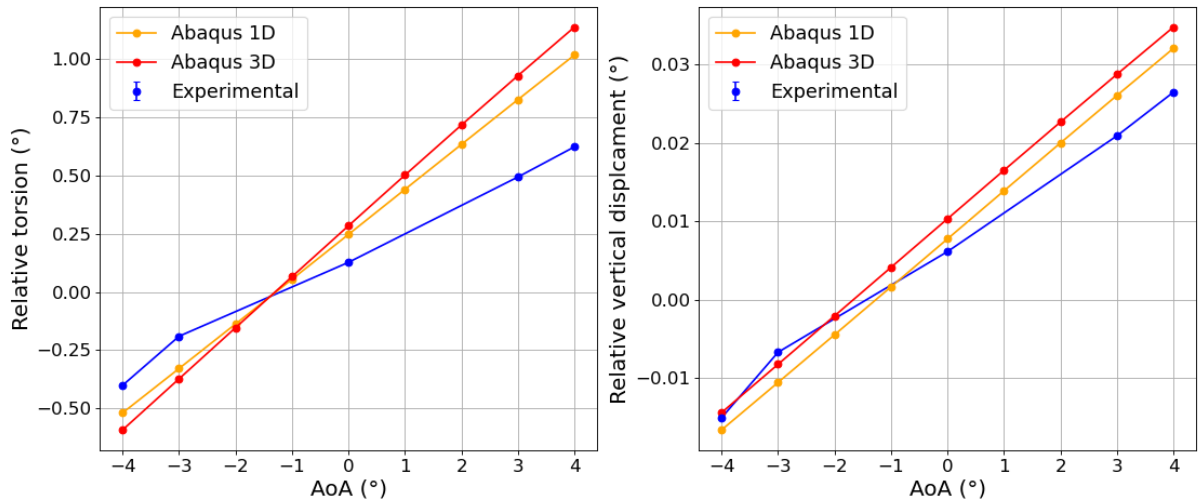


Figure 15: Experimental and numerical values of the torsion (left) and the vertical displacement (right) of the foil at $h/c = 2.76$.

The results show that the two numerical models gives similar results. This validates that 3D composite foils can be modelled with 1D beam elements, instead of 3D solid and 2D shell elements, which are commonly used. Such results are expected, as seen in (Faye et al. 2022), where the equivalent beam approach is validated for punctual load cases.

The numerical models both overestimate the deformation of the foil. Figures 15 shows that the difference on the torsion between the numerical model and the experiment is higher than the difference on the vertical displacement. This could be caused by an over-estimation of the BTC. This would explain why the difference on the torsion is higher than the difference on the vertical displacement. To illustrate the difference on the BTC between the experiments and the numerical models, the torsion is plotted as a function of the vertical displacement, giving a linear curve with a slope proportional

to the BTC of the foil. The slope of the the curve is refereed as the Bend Twist Ratio (BTR) in the rest of the paper. Results showing the BTC estimation are plotted in Figure 16.

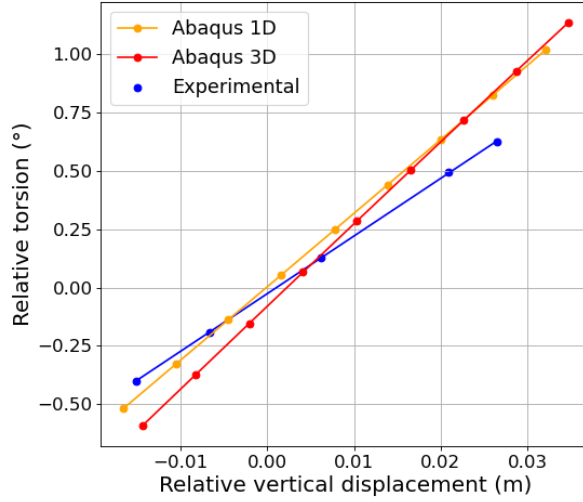


Figure 16: Experimental and numerical bend-twist coupling.

In Figure 16, the slope of the curve relative to the experiments is slightly lower, the values of the different BTR are gathered in Table 4. Considering that the slopes are representative of the BTC, the results shows that the BTC is lower in the experiments than in the numerical models.

When computing the ratio between the experimental and numerical BTC, a mean value of 0.74 is found. This value can be used to reduce the BTC in the numerical model *Abaqus 1D*. To do so, the term K_{45} of the Timoshenko stiffness matrix of the section (see Eq. 6) is multiplied by 0.74. Because of the uncertainties on the manufacture of the experimental foil, it is possible that the composite layup defined during the section analysis (and in *Abaqus 3D*) is not perfectly matching the real structure. Moreover, the BTC term K_{45} is very sensitive to small structural variations (orientation of the UD, composite layup engineering constant) and therefore, the equivalent stiffnesses could be computed correctly but not the BTC.

Table 4: Experimental and numerical value of the bend-twist ratio.

Model	BTR($^{\circ}/m$)	$\frac{\text{Experimental BTR}}{\text{BTR}}$
Experimental	24.7	1.00
Abaqus 3D	31.6	0.78
Abaqus 1D	35.2	0.70

The FSI simulations with the coupling *PUFFIn/Abaqus 1D* are relaunched with a lower BTC coefficient, its original value is reduced by 26%. The new results on the torsion and vertical displacement are given in Figure 17.

After correction of the numerical BTC in *Abaqus 1D*, the slopes and magnitude of the displacement and rotations are closer to the experimental values. Except for the AoA of -3° , the fit between experimental and numerical values is good, this shows the impact of the BTC on the hydroelastic response of the foil. The forces coefficient computed experimentally and numerically are plotted in Figure 18.

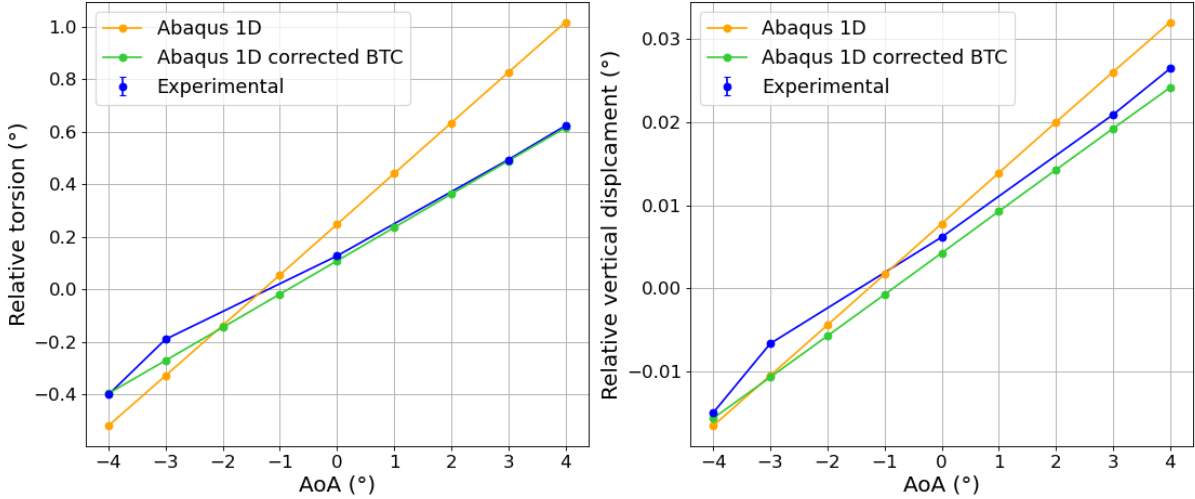


Figure 17: Experimental and numerical values of the torsion (left) and vertical displacement (right) of the foil at $h/c = 2.76$, after correction of the BTC.

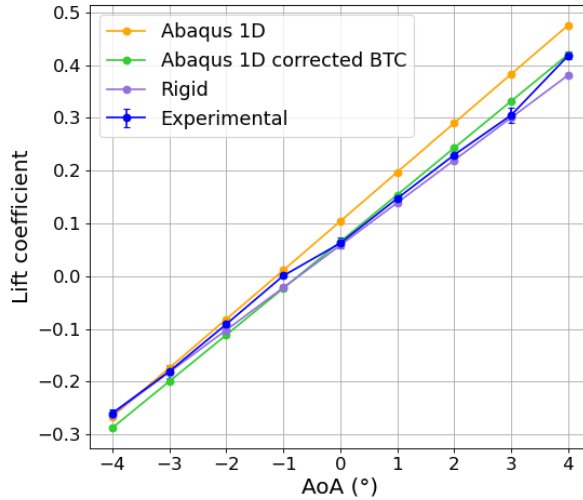


Figure 18: Experimental and numerical values of the lift coefficient of the foil at $h/c = 2.76$, after correction of the BTC.

There is a good match for the positive AoA but for the negative ones, the model without correction fits better the experiments. The major difference between the experimental and numerical results is the trend of the lift coefficients. In the numerical model, the curve is monotonic whereas the experimental curve shows a change of trend between the AoA of -1° and 0° . After analysing the experimental data, an explanation to this would be a problem with the measurement of the forces acting on the foil without any current, probably because of the effects of drift of the balance.

In Figure 18, there is also the lift coefficients obtained on a rigid foil. Because the reference configuration in the experiments is the foil submitted to its buoyancy only, the *Rigid* computations are realized with a mesh of the shape of the foil deformed by its buoyancy (considering the corrected value of the BTC coefficient). The *Rigid* results highlights the effect of the BTC on the lift of the foil. The slope of the C_l curve is higher in the FSI simulations than in the *Rigid* computations, meaning that,

at a given AoA, the deformation of the foil tends to increase its lift. This is due to the BTC which increases the AoA of the foil when it is deformed, and therefore it increases its lift.

In Figure 18, the zero-lift AoA are always negative, this is because at 0° , the foil has a positive AoA induced by the buoyancy and the BTC. Thus, to have zero lift, the initial AoA of the foil has to be negative in order to compensate the AoA induced by the buoyancy.

Finally, Figure 19 illustrates the shape of the deformed foil obtained numerically. The pressure field on the foil is plotted on the initial shape of the foil and on its deformed shape. Figure 19 shows a higher depression on the extrados of the foil in its deformed configuration, highlighting the additional AoA of the foil induced by the BTC.

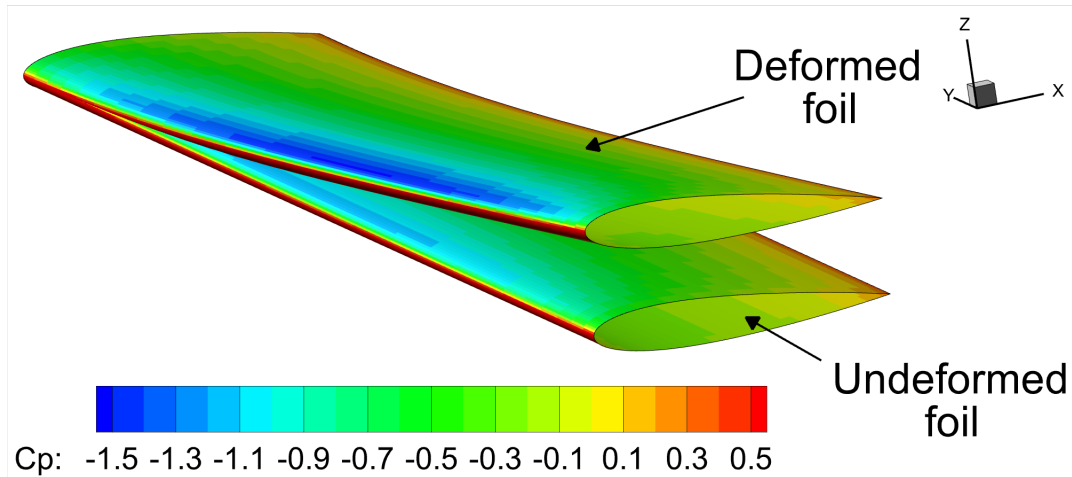


Figure 19: Pressure fields at the surface of the foil computed on its initial shape and deformed shape, for AoA = 4° , $h/c = 2.76$ and $U = 0.8$ m/s

To sum up the numerical results, it is shown that the model *Abaqus 1D* is equivalent to *Abaqus 3D*, which validates that equivalent beam finite elements can be used to describe the structure of composite foils. In addition to that, the experimental results shows that the numerical BTC is overestimated and a reduction of this coefficient by 26% is required to fit the numerical results to the experiments. The computation of the BTC (K_{45}) during the section analysis is very sensitive to the composite layup defined in AbaqusTM. For instance, a variation of 1° of the UD orientation and 5% of the young modulus leads to a 7% variation of the value of K_{45} . The equivalent beam method is suited to describe the hydroelastic response of a foil but a precise modelization of the BTC is mandatory in order to have consistent results.

5. CONCLUSIONS

In this paper, the hydroelastic behavior of a foil submitted to hydrodynamic loads was investigated both numerically and experimentally. Experimental measurements on the foil were realized at the Ifremer flume tank in Boulogne-sur-mer, for two velocities, four immersion and several AoA ranging from -4° to 4° . The foil studied presents a BTC inducing a nose-up twist angle when it is deformed. This means that the hydrodynamic loads acting on the foil increases when it is deformed. This phenomenon is captured experimentally for the two velocities considered, showing the impact of the BTC in FSI of composite foils.

In a second time, the influence of the immersion of the foil is investigated experimentally. For the two

Froude number considered, different behaviors are observed. The higher Froude configuration shows a reduction of the lift coefficients when the foil gets closer to the free-surface. For the lower Froude configuration, the lift coefficient increases as the immersion of the foil is decreasing, until the wave of the foil surges, causing a massive loss of lift.

In this study, two different coupled numerical approaches are presented to simulate the FSI of the foil. For both FSI coupling, the hydrodynamic forces of the foil are computed with the BEM, as implemented in *PUFFIn*. For the first numerical model (*Abaqus 3D*), the structure of the composite foil is studied with 3D solid elements and 2D shell elements. For the second FSI coupling (*Abaqus 1D*), the foil is modelled with 1D finite element equivalent to the 3D model. This method requires a preliminary evaluation of the cross-sections of the foil, which determines the equivalent stiffness of the foil and the potential couplings in the material, such as the BTC.

The numerical results obtained with *Abaqus 3D* and *Abaqus 1D* show a good agreement, which confirms that equivalent beam elements can be used to model the composite foil, resulting into a massive reduction of the computational time. This also validates the method used to project the 3D pressure forces (computed in *PUFFIn*) onto the 1D equivalent beam elements.

At the end of the paper, a validation of the numerical models is presented, considering the experimental measurements as reference values. The comparison shows that the BTC of the numerical models is overestimated, resulting into higher AoA and therefore higher deformation and lift coefficients. A reduction of the BTC of 26% in the numerical model is proposed based on the difference between numerical and experimental results. After the correction, the fit between experimental and numerical results is greatly improved. This highlights the sensitivity of the BTC to the composite layup in the numerical models. Small uncertainties on the material and its orientation may leads to significant variations of the BTC.

The numerical model presented in this paper can be used to study the hydroelastic responses of composite hydrofoils. However, a rigorous description of its structures is mandatory in order to model correctly the couplings in the material.

As a future work, a investigation of the structure of the foil is studied to identify precisely the difference in the numerical models leading to an overestimated BTC. Another perspective is to study a foil with an opposite BTC coefficient, in order to have nose-down twist angle induced by the flexion of the foil.

Acknowledgements

The authors would like to thank the Ifremer of Boulogne-sur-Mer (France), which made this experiments possible. Finally, we also want to acknowledge Jean-Baptiste Marchand of the company Mabe surfboards for the manufacturing of the foils.

References

- Faye, Antoine, N Carrere, Matthieu Sacher, F Hauville, and A Nême (Aug. 2022). “Determination of the equivalent structural properties of a composite hydrofoil”. In.
- Han, Shilei and Olivier Bauchau (July 2015). “Nonlinear Three-Dimensional Beam Theory for Flexible Multibody Dynamics”. In: *Multibody System Dynamics* 34. DOI: 10.1007/s11044-014-9433-8.
- Hodges, Dewey (Apr. 2006). *Nonlinear Composite Beam Theory*. AIAA. ISBN: 978-1-56347-697-6. DOI: 10.2514/4.866821.
- Katz, Joseph and Allen Plotkin (2001). *Low-speed aerodynamics*. Vol. 13. Cambridge university press.

- Liao, Yingqian, Nitin Garg, Joaquim Martins, and Yin Lu Young (Mar. 2019). “Viscous Fluid Structure Interaction Response of Composite Hydrofoils”. In: *Composite Structures* 212. DOI: 10.1016/j.compstruct.2019.01.043.
- Liao, Yingqian, Joaquim Martins, and Yin Young (Apr. 2021). “3-D High-Fidelity Hydrostructural Optimization of Cavitation-Free Composite Lifting Surfaces”. In: *Composite Structures* 268, p. 113937. DOI: 10.1016/j.compstruct.2021.113937.
- (Mar. 2023). “Hydrostructural optimization of single-layer and multi-layer composite lifting surfaces”. In: *Composite Structures* 307, p. 116650. DOI: 10.1016/j.compstruct.2022.116650.
- Liao, Yingqian, Joaquim Martins, and Yin Lu Young (Sept. 2019). “Sweep and Anisotropy Effects on the Viscous Hydroelastic Response of Composite Hydrofoils”. In: *Composite Structures* 230, p. 111471. DOI: 10.1016/j.compstruct.2019.111471.
- Lottati, I. (Nov. 1985). “Flutter and divergence aeroelastic characteristics for composite forward swept cantilevered wing”. In: *Journal of Aircraft - J AIRCRAFT* 22, pp. 1001–1007. DOI: 10.2514/3.45238.
- Marty, Antoine, Christian Berhault, Damblans Guillaume, J.V. Facq, B. Gaurier, Grégory Germain, Thomas Soulard, and Franck Schoefs (Sept. 2021). “Experimental study of hard marine growth effect on the hydrodynamical behaviour of a submarine cable”. In: *Applied Ocean Research* 114, p. 102810. DOI: 10.1016/j.apor.2021.102810.
- Mohammed Arab, Fatiha (Dec. 2020). “Contrôle actif par pression interne des performances hydrodynamiques et de l’apparition de la cavitation d’un hydrofoil composite déformable en composite”. PhD Thesis. UBO.
- Newman, John Nicholas (2018). *Marine hydrodynamics*. The MIT press.
- Oñate, Eugenio (2013). *Structural analysis with the finite element method. Linear statics. Volume 2: Beams, plates and shells*. Vol. 2. Springer.
- PUFFIn documentation* (2023). <https://www.ensta-bretagne.fr/fr/optifoil>.
- Temtching Temou, Vanilla (2020). “Etude expérimentale et numérique des interactions fluide-structure sur des hydrofoils flexibles en composite”. PhD Thesis. UBO. URL: <http://www.theses.fr/2020BRES0043/document>.
- Young, Yin Lu, Nitin Garg, Paul Brandner, Bryce Pearce, Daniel Butler, David Clarke, and Andrew Phillips (Oct. 2017). “Load-Dependent Bend-Twist Coupling Effects on the Steady-state Hydroelastic Response of Composite Hydrofoils”. In: *Composite Structures* 189. DOI: 10.1016/j.compstruct.2017.09.112.